Simulations of Propeller/Airframe Interference Effects Using an Euler Correction Method

T. Q. Dang*
Douglas Aircraft Company, Long Beach, California

An Euler correction method has been used to study propeller effects in airframe-integration studies. In the present method, the propeller is modeled by an actuator disk with proper jump conditions prescribed along the disk. The rotational flowfield behind the propeller is analyzed using the Clebsch formulation of the Euler equations, while the remaining irrotational flowfield is determined with the full-potential method. This method has been successfully implemented into existing axisymmetric nacelle and aft-fuselage/pylon/nacelle codes to study power effects in the presence of a counter-rotating propfan of the pusher type. In the subsonic flow regime where the effect of power is prominent, comparisons of the results obtained using the present method against those of the panel method and experimental data suggest that this simple method is adequate. In the transonic flow regime, calculations indicate that power effects can increase wave drag and trigger earlier shock-induced flow separation.

I. Introduction

RECENT studies confirm that propfan or ultra high bypass (UHB) engine technology offers a significant reduction in aircraft fuel consumption. These studies also identify new problems to the aerodynamicist.[1] For example, one challenge is the integration of the propfan with the airframe so that undesirable aerodynamic interference effects can be minimized. To understand this interaction phenomenon better, it is desirable to have a computational tool that can predict propeller effects on the flowfield around complex configurations.

The concern of an airplane designer is not focused on the details of the blade-to-blade flowfield, but rather on the interference effects generated by the propeller on the airframe. In this case, a simple, computationally easy and inexpensive time-averaged method is preferable to a direct propeller analysis approach. In the former method, the propeller is represented by an actuator disk[2] with proper jump conditions prescribed along the disk. This simplified model for simulating the presence of the propeller has been shown by several authors to be adequate for airframe-integration studies.[3,4]

The flowfield behind a propeller is inherently rotational due to the blade's variable loading characteristics in the spanwise direction. Consequently, an Euler formulation is required for the analysis of the flowfield within the propeller slipstream region behind the actuator disk. There are many recently developed computational methods to solve the Euler equations. Among these, the time-marching finite-volume Euler schemes[5-7] solve for the primitive variables, and have been applied to treat three-dimensional wing/body configurations. Yu et al.[3] and Whitfield and Jameson[4] have successfully employed these time-stepping Euler algorithms to compute the flowfield around complicated three-dimensional propfan configurations.

An alternative procedure for solving the Euler equations is to use Clebsch variables[8-13] as opposed to primitive variables. In this method, the velocity vector is decomposed into a potential part and rotational parts. The potential part can then be determined from the continuity equation, while the rotational parts can be evaluated from the momentum and energy equations. This approach is attractive because the potential part can be determined by solving a modified potential equation using the current state-of-the-art, well-proven, efficient type-dependent relaxation methods.[14-16] Moreover, depending on the size of the rotational region and the complexity of the rotational flowfield, this approach can result in substantial reduction in computer storage requirements and computing times over the time-marching Euler methods.

In this paper, a new theoretical/computational formulation for the analysis of transonic flows around the general three-dimensional configurations in the presence of a propfan is presented. Section II describes the modeling of the propfan by an actuator disk. In Sec. III, an Euler method based on the Clebsch transformation is formulated to analyze the rotational flowfield within the propeller slipstream region behind the actuator disk. Finally, as an illustration of the method, the problem of simulating flows through isolated and aft-fuselage/pylon nacelles-mounted counter-rotating propfan of the pusher type are presented in Secs. IV and V, respectively.

II. Actuator Disk Formulation

Aircraft propulsive devices such as turboprops generate thrust by imparting a change in the momentum flux to a specified mass of air as it passes through the propeller. When the propeller is modeled by an actuator disk,[2] the jump in the flow properties across the disk must be specified. There are a number of choices to prescribe jump conditions, depending on which quantities are given to the designer or are convenient to specify.

The prescription of the jump quantities across the actuator disk is governed by the conservation laws of mass, momentum, and energy. Hence, in principle, the prescription of five jump quantities is allowed. However, since mass is conserved across the propeller, only a maximum of four jump quantities can be specified downstream of the actuator disk. Whitfield and Jameson[4] in their study of propeller-wing interactions in transonic rotational flows, prescribed the force components at the propeller and the increase in the stagnation pressure across the propeller. Yu et al.[3] simulated propeller effects with an actuator disk by prescribing the changes in the stagnation temperature, the stagnation pressure, and the flow angles across the disk.

In the present method, the following quantities are specified behind the actuator disk:

1) The jump in the stagnation enthalpy across the actuator

Received Oct. 17, 1988; revision received April 12, 1989.

*Senior Engineer/Scientist, Aerodynamics Research and Technology; currently, Assistant Professor, Department of Mechanics and Aeronautics, Syracuse University, Syracuse, NY.

disk. This term is related to the radial and circumferential work distribution of the propeller.

2) The jump in the entropy across the actuator disk. This term can be used to describe the degree of irreversibility of the flows as it passes through the propeller, for example, due to the presence of shocks and boundary layers on the propeller blades.

3) The jump in the circumferential velocity or swirl across the actuator disk.

4) The jump in the radial velocity across the actuator disk.

Given these jump quantities across the actuator disk, the inviscid flowfield can be determined by properly incorporating them into the Euler equations. The resulting model can then be used to simulate propeller effects.

III. Theory

The flowfield behind propellers is inherently rotational due to the spanwise variation in the load distribution of most propeller blades. In addition, the flow entering propellers can be highly nonaxisymmetric, due to flow incidence and interference effects caused by various airplane components. Hence, to simulate power effects properly, the equations of motion employed must take into account the above characteristics in determining the flow properties behind the propellers. In this study, the Clebsch representation of the Euler equations is employed to describe the flowfield behind the actuator disk.

A. Flow Analysis Method

In the Clebsch formulation of rotational flows, the vorticity field is expressed in terms of scalar functions[8,12]:

$$\Omega = \sum_n \nabla\sigma_n \times \nabla\lambda_n \tag{1}$$

In Eq. (1), the number of terms in the summation depends on the complexity of the rotational flowfield.

Consider the flowfield behind the actuator disk and within the propeller slipstream. In general, in the stationary frame of reference, the inviscid flowfield can be described by the Crocco's form of the momentum equation,

$$V \times \Omega = \nabla h_o - \frac{a^2}{\gamma}\nabla s \tag{2}$$

A general solution of Eq. (2) is given by

$$\Omega = \Omega_H + \Omega_P \tag{3}$$

where Ω_H is the homogeneous solution and Ω_P is the particular solution of Eq. (2), namely,

$$V \times \Omega_H = 0 \tag{4}$$

$$V \times \Omega_P = \nabla h_o - \frac{a^2}{\gamma}\nabla s \tag{5}$$

Consider the particular solution. This component of the vorticity field is related to the stagnation enthalpy and the entropy gradients introduced to the flow as it passes through the propeller. Following the general form suggested by Clebsch in Eq. (1), this component of the vorticity field can be expressed as[9,10,12,17]

$$\Omega_P = \nabla h_o \times \nabla t - \nabla s \times \nabla\tau \tag{6}$$

where h_o is the stagnation enthalpy and s the entropy. For steady inviscid and adiabatic flow, the energy equation combined with the momentum equation requires

$$V \cdot \nabla h_o = 0 \tag{7}$$

$$V \cdot \nabla s = 0 \tag{8}$$

On substituting Eqs. (6–8) into Eq. (5), along with the use of vector identities, the governing equations for the Clebsch variables t and τ are obtained:

$$V \cdot \nabla t = 1 \tag{9}$$

$$V \cdot \nabla\tau = \frac{a^2}{\gamma} \tag{10}$$

Conceptually, the Clebsch variable t is the classical Darwin-Lighthill-Hawthorne drift function.[17–19] Physically, constant t surfaces in the flowfield are material surfaces, and the variation of t from streamline to streamline is directly connected to the stretching and tipping of the vortex filaments associated with the stagnation enthalpy variation in the flowfield. The Clebsch variable τ is similar to the Darwin-Lighthill-Hawthorne drift function. It is used to describe the stretching and tipping of the vortex filaments associated with the entropy variation in the flowfield.

Finally, consider the homogeneous solution. Classically, this component of the vorticity field is termed the Beltrami vorticity and can be represented by[10,13,20]

$$\Omega_H = \nabla\alpha \times \nabla G \tag{11}$$

where $\alpha \equiv \theta - f(r,x)$ can be interpreted as the "cascade" stream function and satisfies the kinematic condition

$$V \cdot \nabla\alpha = 0 \tag{12}$$

On substituting Eqs. (11) and (12) into Eq. (4), along with the use of vector identities, the governing equation for G is obtained:

$$V \cdot \nabla G = 0 \tag{13}$$

In the axisymmetric flow case, the Clebsch variable G can be shown to be the fluid angular momentum per unit mass,[10] while in the general three-dimensional case G is related to the fluid angular momentum per unit mass and the nonaxisymmetric characteristics of the flowfield.[20]

In summary, the vorticity field can be expressed in terms of the Clebsch variables as

$$\Omega = \nabla h_o \times \nabla t - \nabla s \times \nabla\tau + \nabla\alpha \times \nabla G \tag{14}$$

and, hence, a Clebsch representation of the velocity vector is

$$V = \nabla\phi + (h_o - h_{o\infty})\nabla t - (s - s_\infty)\nabla\tau - G\nabla\alpha \tag{15}$$

Note that the curl of Eq. (15) gives Eq. (14), as it should. Finally, the continuity equation is employed to determine the potential part in the velocity expression. For steady flow, the continuity equation is

$$\nabla \cdot (\rho V) = 0 \tag{16}$$

On substituting Eq. (15) into Eq. (16), the potential part ϕ can be calculated from

$$\nabla \cdot (\rho\nabla\phi) = -\nabla \cdot [\rho(h_o - h_{o\infty})\nabla t - \rho(s - s_\infty)\nabla\tau - \rho G\nabla\alpha] \tag{17}$$

The speed of sound and the density can be related to the local flow properties by means of the energy equation and the entropy relationship:

$$a^2 = (\gamma - 1)(h_o - h_{o\infty}) + \left[\frac{1}{M_\infty^2} + \frac{\gamma - 1}{2}(1 - q^2)\right] \tag{18}$$

$$\rho = e^{-(s - s_\infty)}\left[\left(\frac{h_o}{h_{o\infty}}\right)\frac{1 + \frac{\gamma - 1}{2}M_\infty^2}{1 + \frac{\gamma - 1}{2}M^2}\right]^{\frac{1}{\gamma - 1}} \tag{19}$$

where M_∞ is the freestream Mach number, M the local Mach number, q the total velocity, and γ the ratio of the specific heats.

In principle, the flowfield can be computed by solving iteratively between the governing equation of the potential part, Eq. (17), and the governing equations of the rotational parts, Eqs. (7–10), (12), and (13), subjecting them to appropriate boundary conditions.

B. Discussions of Boundary Conditions

To determine the flowfield, the governing equations of the potential part and the rotational parts must be solved with proper boundary conditions. Special attention must be paid to the specifications of boundary conditions at the actuator disk and along the propeller slipstream.

The rotational parts are governed by partial differential equations of the hyperbolic (or convective) type. In order to solve them, boundary conditions need to be prescribed on the actuator disk surface. In the present method, the boundary conditions for the Clebsch variables h_o and s are explicitly specified, as discussed in Sec. II. For convenience and without any loss of generality, the potential part ϕ is taken to be single-valued on the actuator disk surface. As a result, the boundary conditions for the remaining Clebsch variables, t,τ, α, and G, at the actuator disk are chosen to produce the specified jump in the radial and circumferential velocities. Using Eq. (15), the boundary values of these Clebsch variables must satisfy the following conditions:

$$\Delta V_r = (h_o - h_{o\infty})\frac{\partial t}{\partial r} - (s - s_\infty)\frac{\partial \tau}{\partial r} + G\frac{\partial f}{\partial r} \tag{20}$$

$$\Delta r V_\theta = (h_o - h_{o\infty})\frac{\partial t}{\partial \theta} - (s - s_\infty)\frac{\partial \tau}{\partial \theta} - G \tag{21}$$

The potential function is governed by a mixed elliptic-hyperbolic equation. As discussed earlier, the boundary conditions for the rotational parts are chosen to represent all of the specified jump conditions across the actuator disk so that the potential function is continuous across this surface. In addition, to model propeller-tip effects, these prescribed jump quantities are taken to vanish at the tip of the actuator disk. Under these conditions, the flow is smooth across the propeller slipstream and no special treatment on the potential function is required on this stream surface. Consequently, a single potential function is employed for the entire flowfield with the same type of boundary conditions applied at the far field and along the nacelle surface as in the full-potential method.[15]

IV. Application: Isolated Nacelle-Mounted Counter-Rotating Propeller of the Pusher Type

As an illustration of the method, the problem of simulating flow through an "ideal" isolated nacelle-mounted counter-rotating propfan of the pusher type in axisymmetric flow is presented. In an ideal counter-rotating propfan, the forward propeller induces a swirl to the oncoming flow, and the aft propeller removes it completely. This assumption implies that the jump in the circumferential velocity across the actuator disk is zero. Hence, from Eq. (21), the boundary value for G at the actuator disk surface is zero. But since G is conserved along a streamline as required by its governing equation, Eq. (13), G is zero everywhere in the flowfield. Furthermore, the flow through an ideal counter-rotating propfan is assumed to be isentropic, and the jump in the radial velocity is assumed to be zero.

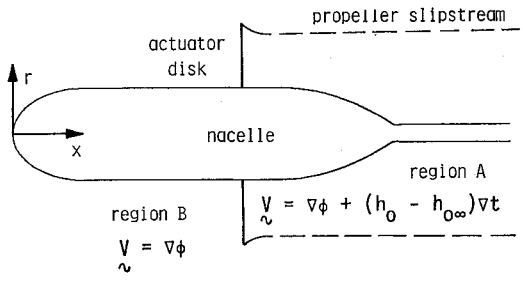

Fig. 1 Actuator disk model of an ideal counter-rotating propeller.

Consequently, it is appropriate to model the presence of a counter-rotating propfan with a single actuator disk across which there exists only a jump in the stagnation enthalpy. To determine the flowfield, the flow domain is divided into two parts (Fig. 1). Region A comprises of the flowfield behind the actuator disk within the propeller slipstream, and region B is the remaining flowfield. In region A, the flow is generally rotational due to the radial variation in the stagnation enthalpy jump across the actuator disk. Conceptually, the presence of the actuator disk introduces rings of vorticity centered about the nacelle centerline. In region B, assuming irrotational flow far upstream, the flowfield can be formulated in terms of a potential function.

From Sec. III, the expression for the velocity vector reduces to

$$V = \nabla\phi + (h_o - h_{o\infty})\nabla t \tag{22}$$

where the rotational part vanishes in region B. The flowfield is calculated by solving the continuity equation for the potential function and the Clebsch representation of the momentum and energy equations for the rotational part, subjecting them to appropriate boundary and matching conditions between the two regions.

A. Solution Method for the Rotational Part

The rotational part in the expression for the velocity is updated by solving the convective equations (7–9), for h_o and t. Given the solution of the velocity field from the previous iteration, these equations reduce to linear first-order partial differential equations of the hyperbolic type. In order to solve them, boundary conditions for h_o and t need to be prescribed at the actuator disk.

In the present formulation, the boundary condition for the stagnation enthalpy jump across the actuator disk is given. In practice, however, it is more useful to prescribe the propeller thrust-loading coefficient. Using the one-dimensional incompressible flow Froude-Rankine momentum theorem,[21] the increase in the stagnation enthalpy across the propeller can be related to the thrust-loading coefficient T/QA_d by[20]

$$\Delta h_o(r) = \frac{T/QA_d}{(4\pi/A_d)\int_{R_{\text{hub}}}^{R_{\text{tip}}} F(r)r\,dr} F(r) \tag{23}$$

where $F(r)$ is the propeller loading characteristics. In Eq. (23), T is the total thrust produced by the propeller, Q is the dynamic pressure, A_d is the propeller frontal area, and R_{hub} and R_{tip} are the propeller hub and tip radius, respectively.

Figure 2 illustrates two propeller load distributions studied in this paper. In the hub-loaded blading case, most of the work done by the propeller blades on the fluid is accomplished near the hub region. The opposite is true for the tip-loaded blading case. Note that in both cases, the jump in the stagnation enthalpy is chosen to vanish at the hub and tip in order to simulate the presence of the nacelle boundary-layer and propeller-tip effects, respectively. Also shown in Fig. 2 is the propeller load distribution of the free-vortex type. In this case, the work is equally distributed from the hub to the tip. The present method cannot handle this type of propeller load distribution because of the presence of discontinuities in flow properties along the propeller slipstream. Reference 22 sum-

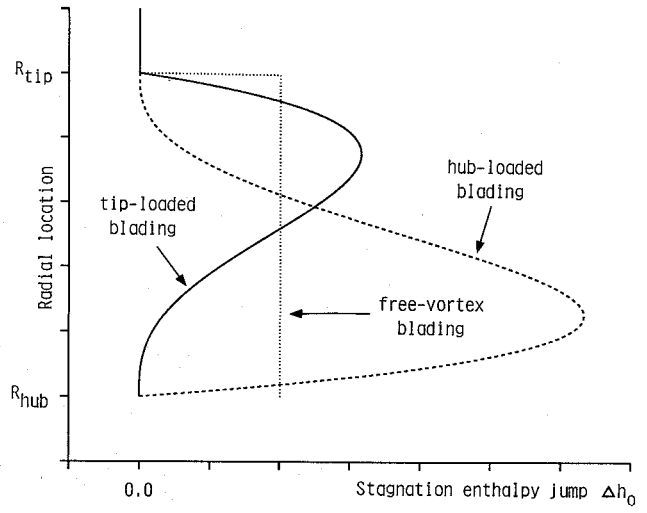

Fig. 2 Propeller load distributions.

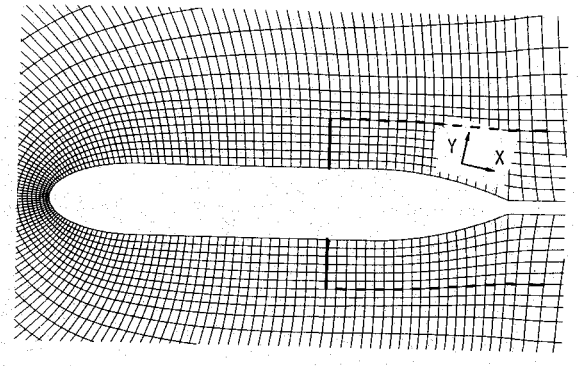

Fig. 3 Partial grid distribution about an isolated nacelle.

marizes a method of handling propellers of the free-vortex blading type. Numerical simulations using this method confirm that Eq. (23) is accurate in both the practical subsonic and transonic flow regimes.

The boundary condition for the drift time at the actuator disk can be obtained from the assumed zero-jump condition in the radial velocity across the actuator disk. On using Eq. (20), along with the fact the G vanishes everywhere in the flowfield and the isentropic flow assumption, this condition implies

$$t(x_{\text{disk}},r) = \text{const} = 0 \tag{24}$$

In the present study, the Clebsch variables h_o and t are updated by solving Eqs. (7) and (9) analytically using small perturbation approximations that are similar to those successfully employed to model the vorticity field generated behind shocks.[9] In theory, these types of approximations can be shown to be valid if[20]

$$\frac{1}{2}\left(\frac{T}{QA_d}\right) \ll 1.0 \tag{25}$$

Following the technique employed in Ref. 9, the stagnation enthalpy is assumed to be convected along the C-type mesh lines (Fig. 3), which are approximately the streamlines, and the governing equation for the Clebsch variable t is linearized about u^*, a characteristics axial velocity at the disk. Here u^* is derived using the one-dimensional incompressible Froude-Rankine momentum theory[21] and can be shown to be[20]

$$u^* = \frac{1}{2}\left(1 + \sqrt{1 + \frac{T}{QA_d}}\right) \tag{26}$$

On linearizing Eq. (9) about u^*, the following is obtained:

$$\frac{\partial t}{\partial x} = \frac{1}{u^*} \tag{27}$$

Moreover, from the zero-jump condition in the radial velocity across the actuator disk and from the fact that the disk surface is located at constant axial distance, the following must hold

$$\frac{\partial t}{\partial r} = 0 \tag{28}$$

B. Solution Method for the Potential Part

As mentioned in Sec. III, the potential part ϕ is chosen to be single-valued at the boundary interfaces between region A and B. Taking advantage of this choice, the potential part ϕ can be determined using an existing efficient and reliable finite-volume full-potential flow solver[15] with some minor modifications. In the finite-volume formulation, the potential function at the $(n+1)$th iterative level is updated using

$$L^n(\phi^{n+1} - \phi^n) = -Res^n \tag{29}$$

where L is the potential equation operator and Res the residual of the continuity equation evaluated at the nth iterative level. The discretization procedure for the residual Res used in the finite-volume formulation written in the computational space is

$$Res \equiv u_Y \delta_X[r(\rho hU + P)] + \mu_X \delta_Y[r(\rho hV + Q)] \tag{30}$$

where μ is the averaging operator, δ the differencing operator, h the Jacobian of the transformation, and (U,V) the contravariant velocity vector. In this equation, the artificial viscosity fluxes P and Q are added in order to stabilize the algorithm in the supersonic regions.

When the present power method is included, the general forms of the operator L and the artificial viscosity fluxes remain unchanged. The only modifications involved are in the evaluation of the cell-averaged velocity, speed of sound, and density that appear in these expressions. Based on the approximations discussed in Sec. IV.A, the velocity vector takes on the form

$$V = \nabla\phi + \frac{\Delta h_o}{u^*}\hat{e}_x \tag{31}$$

The expression for the speed of sound in Eq. (18) remains unchanged, and the density takes on the isentropic form of Eq. (19).

Given the thrust-loading coefficient and the propeller load distribution function, Eqs. (23) and (26) are used to compute the radial distribution of the stagnation enthalpy jump across the actuator disk and the characteristics axial velocity, respectively. The approximations discussed in Sec. IV.A are then applied to the stagnation enthalpy field in region A. This is accomplished by setting Δh_o to be constant along the Y-mesh lines from the actuator disk to the downstream boundary (Fig. 3). This enthalpy field is kept fixed during the calculation. Consequently, the rotational term in Eq. (31) becomes a prescribed quantity, and the entire calculation reduces to solving the continuity equation for the potential function.

C. Results

The method presented in this section has been implemented into an axisymmetric finite-volume full-potential code[15] to compute power effects for isolated nacelles at 0 deg angle of attack. Figure 3 shows the nacelle geometry, the actuator disk location, and the grid distribution employed in the following calculations. Generation of the computational grid is accomplished using hybrid conformal-mapping/algebraic techniques

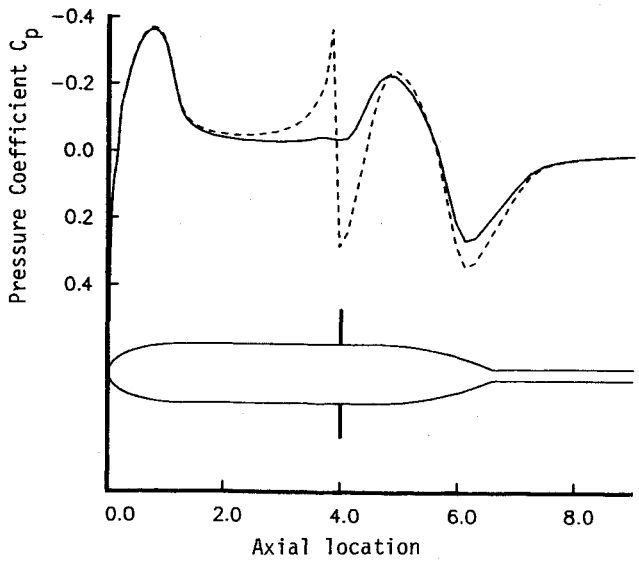

Fig. 4 Comparison of nacelle surface pressure distributions at $M_\infty = 0.8$ and $T/QA_d = 0.24$ ($x_{disk} = 4.0$).

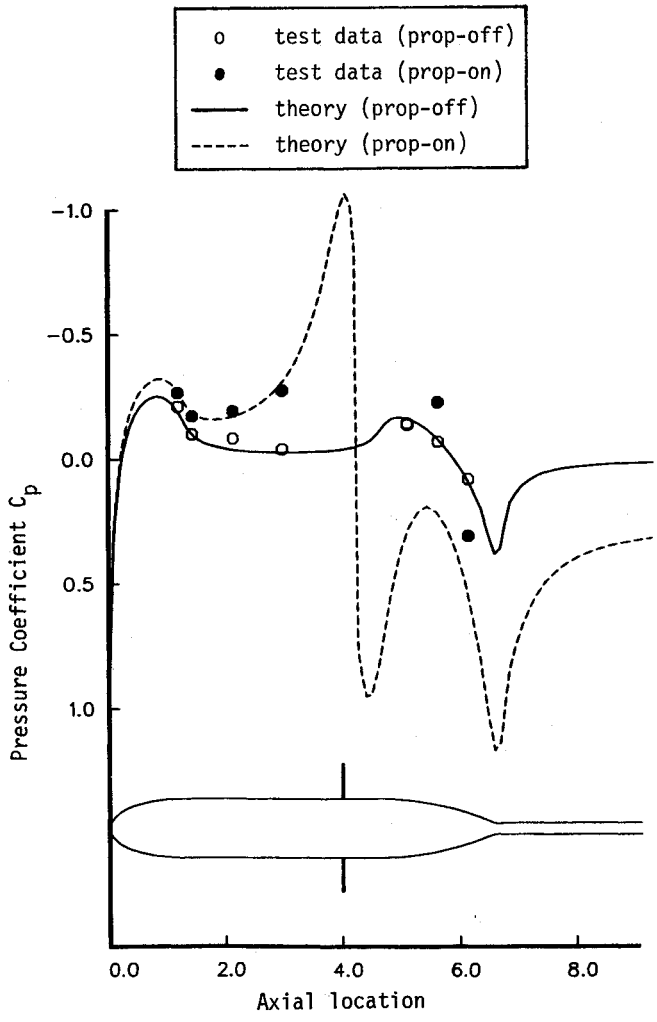

Fig. 5 Comparison of nacelle-surface pressure distributions at $M_\infty = 0.2$ and $T/QA_d = 4.0$ ($x_{disk} = 4.0$).

of Halsey.[23] This method conforms grid lines to a specified actuator disk location and size, along with the option of conforming the grid lines to an assumed location of the slipstream based on the Froude-Rankine analysis.[20]

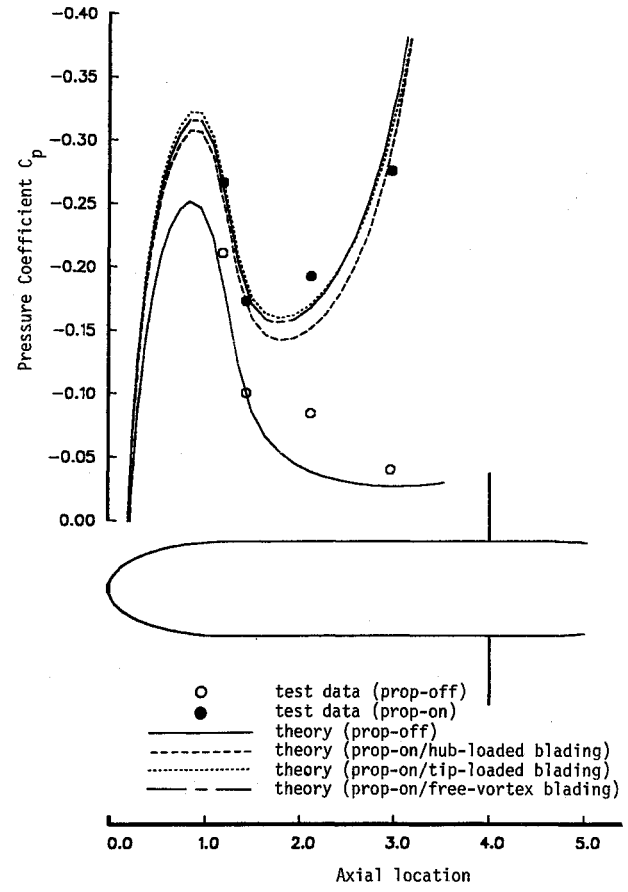

Fig. 6 Effects of propeller loading characteristics on nacelle-surface pressure distributions at $M_\infty = 0.2$ and $T/QA_d = 4.0$ ($x_{disk} = 4.0$).

Figure 4 shows a comparison of the pressure distribution on the nacelle surface between the propeller-off and propeller-on cases at a typical cruising condition ($M_\infty = 0.8$ and $T/QA_d = 0.24$). The propeller loading characteristics employed in this example is of the tip-loaded blading and is typical of many advanced propeller blades. As expected, the effects of power are to accelerate the flow in front of the propeller and to produce an increase in static pressure across the propeller. Behind the actuator disk, it is important to note that the velocity cannot be inferred directly from pressure plots because the stagnation quantities in front and behind the actuator disk are different. Figure 4 indicates that in the absence of swirl, the computed static pressure approaches the freestream condition as required by the radial equilibrium condition.

Figure 5 illustrates a comparison of the pressure distribution on the nacelle surface as predicted by the present method against the test data at a practical low-speed condition ($M_\infty = 0.2$ and $T/QA_d = 4.0$). Note that the thrust-loading coefficient level in this case is well outside the range of applicability of the present method [see Eq. (25)]. This figure indicates that the pressure distribution on the nacelle surface in front of the propeller is predicted well. Behind the propeller, the small-perturbation approximation breaks down and the results compare poorly with the test data.

To investigate the influence of the propeller loading characteristics on the flowfield outside the propeller slipstream, a comparison of the nacelle-surface pressure distribution in front of the actuator disk for three different types of propeller loading is shown in Fig. 6. The tip- and hub-loaded blading results are obtained using the present method, and the free-vortex blading result is obtained using the potential/multi-energy flow method.[22] The thrust-loading coefficient employed in these calculations is 4, well outside the range of applicability of the present method, but valid for the poten-

tial/multienergy flow method. This figure indicates that the flow region upstream of the actuator disk is relatively insensitive to the propeller loading characteristics. Similar comparison was carried out in the transonic flow regime where the thrust-loading coefficient is small. In this case, the computed nacelle-surface pressure distributions for these three types of propeller loading are not only virtually identical upstream of the actuator disk, but also downstream of the actuator disk. This study suggests that the propeller loading characteristics do not play an important role in the prediction of propeller/airframe interference effects.

V. Application: Aft-Fuselage/Pylon/Nacelle-Mounted Counter-Rotating Propeller of the Pusher Type

In this section, the method used for simulating propeller effects in the axisymmetric case is generalized to analyze the flowfield around an aft-fuselage/pylon/nacelle-mounted counter-rotating propeller of the pusher type. This method has been successfully implemented into a transonic full-potential code used to analyze the flowfield about an aft-fuselage/pylon/nacelle configuration.[24]

In practice, the flow entering the propeller can have swirl and can be highly nonaxisymmetric due to flow incidence and interference effects caused by various airplane components. Hence, the changes in the tangential and radial velocities across the propfan are generally nonzero and have large variation in both the radial and circumferential directions. However, for simplicity, the present study assumes the flowfield behind the actuator disk to have no jump in either the radial or the circumferential velocities. Furthermore, the jump in the stagnation enthalpy is assumed to vary in the radial direction only. Under these assumptions, the flowfield within the propeller slipstream behind the actuator disk can be described by the same formulation as in the axisymmetric case described in Sec. IV. In the high thrust-loading-coefficient simulation cases, such as the takeoff and climbing conditions, the approximations used to analyze the flowfield within the propeller slipstream behind the actuator disk is not accurate. However, this is not crucial, since for this particular configuration, the main region of interest to the designers is on the pylon and the fuselage, which do not lie within the rotational flow region.

Figure 7 illustrates comparisons of the pressure distribution on the pylon between the propeller-off and propeller-on cases for configuration A at the cruising and the onset of shock-induced flow separation conditions. Figure 8 shows similar comparisons for configuration B. In these examples, the thrust-loading coefficients are chosen to be equal to the thrust required to balance the predicted drag at these flight conditions. The magnitude of the thrust-loading coefficients employed in these calculations is within the range of applicability of the present method, namely Eq. (25). Figure 7 indicates that when shocks appear on the pylon near the propfan, the effect of power is to increase the shock strength and move it further downstream, resulting in higher wave drag and earlier onset of shock-induced flow separation. On the other hand, when shocks appear far away from the propfan, such as in the configuration B design (Fig. 8), the wave drag in the propeller-off and propeller-on cases is expected to be the same.

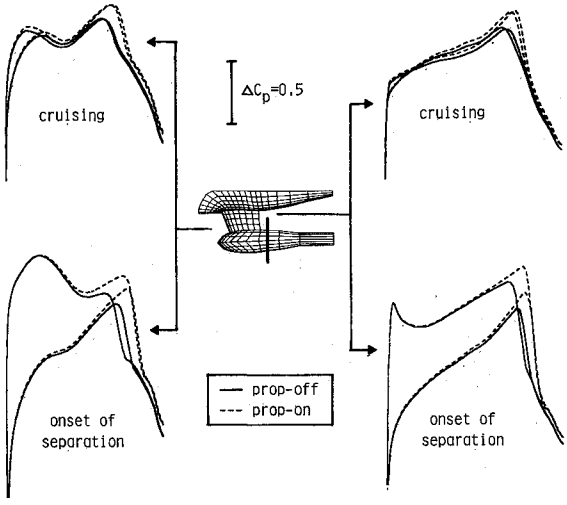

Fig. 7 Comparison of pylon pressure distributions for configuration A at the cruising and the onset of shock-induced flow separation conditions.

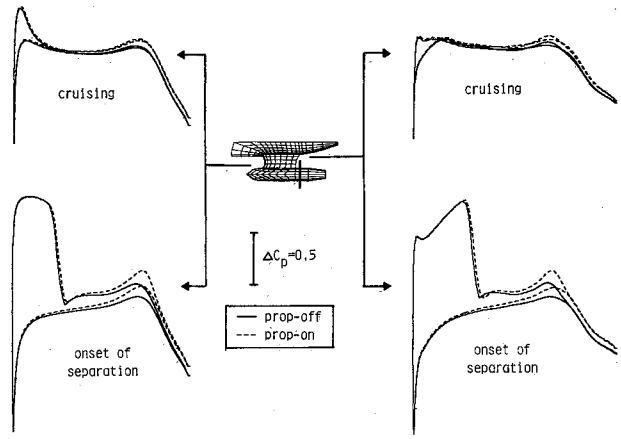

Fig. 8 Comparison of pylon pressure distributions for configuration B at the cruising and the onset of shock-induced flow separation conditions.

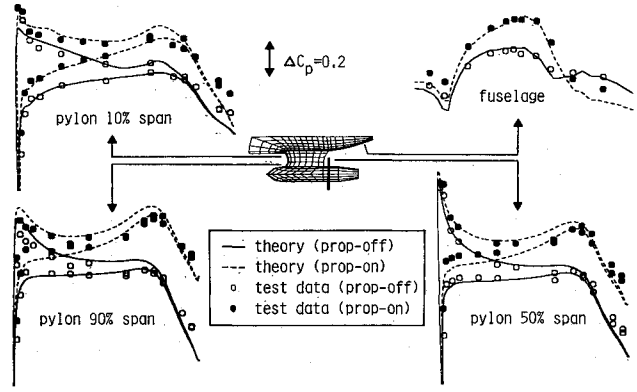

Fig. 9 Comparison of pylon and fuselage pressure distributions for configuration B at $M_\infty = 0.2$, $\alpha = -3$ deg and $T/QA_d = 2.0$.

To validate the method, a comparison of its predictions with experiment is necessary. Unfortunately, no high-speed test data is available and the low-speed test data is available for a different configuration. Although the calculation method is limited to a pylon/nacelle mounted on a body infinite in the upstream direction, test results are available for two configurations at $M_\infty = 0.2$ and $T/QA_d = 2.0$: a wing-fuselage pylon/nacelle with and without a tail. The experimental data for the configuration without a tail do not agree with the calculations for the power-off condition. However, the power-off test data for the configuration with a tail do agree with the calculations, using a corrected value for the freestream angle of attack. Accordingly, the power-on test data for this configuration are compared with the calculations in Fig. 9, and the agreement is very good. This indicates the ability of the method to predict the pressure increments due to power. These results also show that the effect of power is very prominent in the practical low-speed regime: the pressure level is modified over the entire aft portion of the airplane.

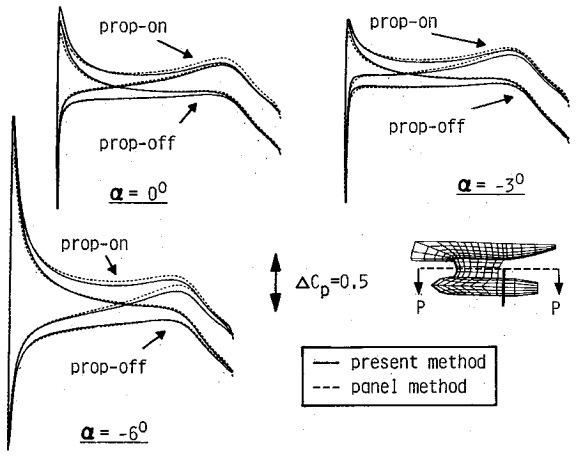

Fig. 10 Comparison of pylon pressure distributions (station P-P) as a function of angle of attack (configuration B at $M_\infty = 0.2$ and $T/QA_d = 2.0$).

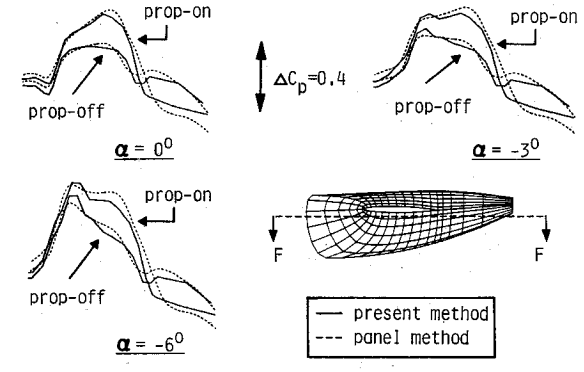

Fig. 11 Comparison of fuselage pressure distributions (station F-F) as a function of angle of attack (configuration B at $M_\infty = 0.2$ and $T/QA_d = 2.0$).

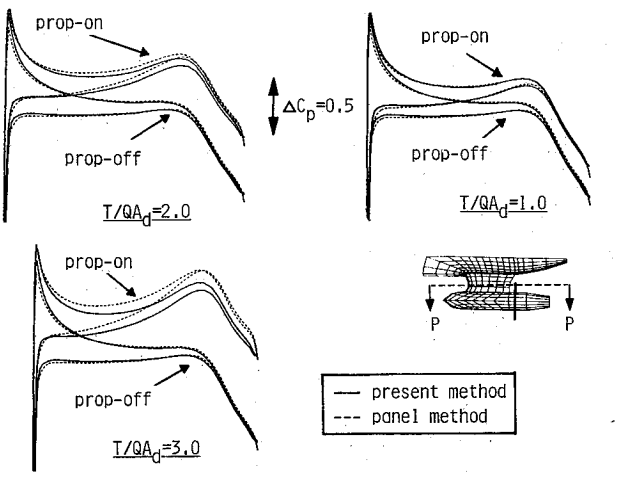

Fig. 12 Comparison of pylon pressure distributions (station P-P) as a function of thrust-loading coefficient (configuration B at $M_\infty = 0.2$ and $\alpha = -3$ deg).

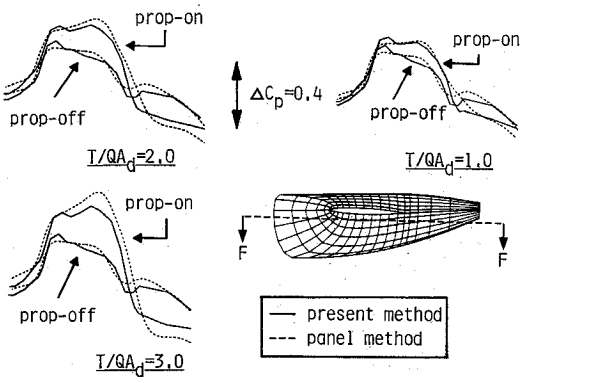

Fig. 13 Comparison of fuselage pressure distributions (station F-F) as a function of thrust-loading coefficient (configuration B at $M_\infty = 0.2$ and $\alpha = -3$ deg).

Finally, Figs. 10–13 show comparisons of the pressure coefficients on the pylon and on the fuselage between the present method and the panel method[25–27] as a function of angle of attack and thrust-loading coefficient. In the panel method, the mutual aerodynamic interference effects between the propeller and the airframe are approximated by superimposing the time-averaging isolated propeller solution to a "standard" panel solution[27] for the remaining part of the aircraft. This panel method and the method described in this paper employ very different models and approximations to simulate propeller/airframe interference effects.

Figures 10 and 11 illustrate comparisons of the pressure coefficients obtained using these two methods on the pylon and along the fuselage as a function of angle of attack, respectively. Clearly, the agreement in the overall trend, as well as magnitude, is excellent. Figures 12 and 13 show the same comparisons, but as a function of thrust-loading coefficient. Here, the overall trend between these two methods is the same, but the magnitude starts to deviate as the thrust-loading coefficient increases.

As the overall trend in these two solutions is essentially the same, and since the panel method and the present method model the propeller bound- and shed-vorticity structures very differently, these comparisons indicate that the propeller loading characteristics appear to be unimportant for this application. Here, the power effect is characterized by the suction of the propeller or the amount of the propeller slipstream contraction, which is a strong function of the thrust-loading coefficient. Since both methods make approximations in matching the specified thrust-loading coefficient, it is not surprising that the agreement between their solutions worsens as the thrust-loading coefficient increases.

VI. Conclusions and Recommendations

A new theory has been formulated to simulate propeller effects for airframe-integration studies. The propeller is represented by an actuator disk with proper jump conditions prescribed along the disk. The Clebsch formulation of the Euler equations is employed to analyze the rotational flowfield behind the propeller. In this approach, the velocity vector is divided into potential and rotational parts, written in terms of scalar functions. The potential part is determined from the continuity equation using a modified version of an existing full-potential solver. The governing equations of the rotational parts are obtained from the momentum and energy equations. In this study, these equations are solved analytically based on small-perturbation approximations.

The present method for simulating propeller effects has been successfully incorporated into existing axisymmetric nacelle and three-dimensional transonic codes to simulate the presence of a counter-rotating propfan of the pusher type. The following conclusions are drawn from this study:

1) In the transonic flow regime, the thrust-loading coefficient is small, and the effect of power can be handled adequately using a perturbation method. Calculations indicate that power effects can increase wave drag and trigger earlier shock-induced flow separation.

2) In the subsonic flow regime, the thrust-loading coefficient is high and power effects are prominent. The present

method predicts the flowfield within the propeller slipstream approximately, but appears to predict the remaining flowfield well, both in trend and in magnitude, as shown by the comparisons with the limited amount of experimental data available and with the panel method.

3) It appears that the radial variation in the stagnation enthalpy jump across the actuator disk is not important, at least for the configurations considered. The structure of the propeller bound/shed vorticity field does not appear to be important in propeller/airframe integration studies.

The present method can be further improved by solving the governing equation for h_o numerically. In this case, the propeller slipstream is explicitly captured during the calculation. The method can then be used to handle large angle-of-attack cases more accurately and other grid topologies. Finally, the modeling of the overall propeller efficiency and the flowfield behind a single propeller can easily be incorporated into the present method by including the additional rotational terms in the expression for the velocity vector shown in Eq. (15). These terms are used to account for the entropy increase across the actuator disk and the swirl introduced into the flowfield by a single propeller. The same approximations described in Sec. IV.A can be applied to evaluate these two rotational terms.

Acknowledgments

The work reported in this paper was conducted under the sponsorship of the Independent Research and Development Program of the McDonnell Douglas Corporation. The author would like to acknowledge L. T. Chen and K. C. Yu for their assistance in the grid-generation method and the unpowered version of the potential-flow solver.

References

[1]Page, M. A., Ivey, D. M., and Welge, H. R., "Ultra High Bypass Engine Applications to Commercial and Military Aircraft," Society of Automotive Engineers Paper 861720, 1986.

[2]Horlock, J. H., *Actuator Disk Theory*, McGraw-Hill, New York, 1978.

[3]Yu, N. J., Samart, S. S., and Rubbert, P. E., "Flow Prediction for Propfan Configurations Using Euler Equations," AIAA Paper 84-1645, June 1984.

[4]Whitfield, D. L. and Jameson, A., "Three-Dimensional Euler Equation Simulation of Propeller-Wing Interaction in Transonic Flow," AIAA Paper 83-0236, 1983.

[5]Jameson, A., Schmidt, W., and Turkel, E., "Numerical Solutions of the Euler Equations by Finite-Volume Methods Using Runge-Kutta Time-Stepping Schemes," AIAA Paper 81-1259, June 1981.

[6]Jameson, A. and Baker, T. J., "Multigrid Solution of the Euler Equations for Aircraft Configurations," AIAA Paper 84-0093, Jan. 1984.

[7]Rizzi, A., "Damped Euler-Equation Method to Compute Transonic Flow Around Wing-Body Combinations," *AIAA Journal*, Vol. 20, Oct. 1982, pp. 1321–1328.

[8]Lamb, H., *Hydrodynamics*, Dover, New York, 1960, pp. 248–249.

[9]Dang, T. Q. and Chen, L. T., "An Euler Correction Method for Two- and Three-Dimensional Transonic Flows," AIAA Paper 87-0522, Jan. 1987.

[10]Dang, T. Q., "A Three-Dimensional Blade Design Method to Control Secondary Flow," Ph.D. Thesis, Dept. of Aero/Astro, MIT, Cambridge, MA, June 1985.

[11]McCune, J. E. and Hawthorne, W. R., "The Effects of Trailing Vorticity on the Flow Through Highly Loaded Cascades," *Journal of Fluid Mechanics*, Vol. 74, April 1976, pp. 721–740.

[12]Hawthorne, W. R., "On the Theory of Shear Flow," MIT GTL Rept. 88, 1966.

[13]Hawthorne, W. R., McCune, J. E., Mitchell, N. A., and Tan, C. S., "Nonaxisymmetric Flow Through an Annular Actuator Disk: Inlet Distortion Problem," *ASME Journal of Engineering for Power*, Vol. 100, Oct. 1978, pp. 604–617.

[14]Jameson, A. and Caughey, D. A., "A Finite-Volume Method for Transonic Potential-Flow Calculatiions," *Proceedings of the AIAA 3rd Computational Fluid Dynamics Conference*, AIAA, New York, 1977, pp. 35–54.

[15]Shmilovich, A. and Caughey, D. A., "On Transonic Flow Computations About Airfoils, Axisymmetric Projectiles, and Nacelles in Free Air and in Wind Tunnels," Douglas Aircraft Rept. MDC J3852, Oct. 1985.

[16]Chen, L. T., Vassberg, J. C., and Peavey, C. C., "A Transonic Wing-Body Flowfield Calculation with an Improved Grid Topology," *AIAA Journal*, Vol. 23, Dec. 1985, pp. 1877–1884.

[17]Hawthorne, W. R., "The Actuator Duct Representation of Turbomachinery Blade Rows," Dept. of Engineering, University of Cambridge, England, CUED/A—Turbo/TR 119, 1983.

[18]Darwin, C., *Notes on Hydrodynamics*, Proceedings of the Cambridge Philosophical Society, Vol. 49, 1953, pp. 352–254.

[19]Lighthill, M. J., "Drift," *Journal of Fluid Mechanics*, Vol. 1, 1956, pp. 31–53; also "Corrigenda to Drift," *Journal of Fluid Mechanics*, Vol. 2, 1957, pp. 311–312.

[20]Dang, T. Q., "Simulation of Propeller Effects Using an Actuator Disk and the Euler-Clebsch Method," Douglas Aircraft Co., Rept. MDC J4953, 1987.

[21]Dommash, Sherby, and Connolly, *Airplane Aerodynamics*, Pitman, New York, 1967.

[22]Zaretsky, B., Dang, T. Q., Shmilovich, A., and Halsey, N. D., "Calculation of Propeller Effects on Axisymmetric Nacelles With and Without Inlets," Douglas Aircraft Co., Rept. MDC J4920, Oct. 1986.

[23]Halsey, N. D., "Use of Conformal Mapping in Grid Generation for Complex Three-Dimensional Configurations," *AIAA Journal*, Vol. 15, Oct. 1987, pp. 1286–1291.

[24]Chen, L. T., Yu, K. C., and Dang, T. Q., "A Transonic Computational Method for Calculating Flowfields About an Aft-Fuselage Mounted Nacelle/Pylon Configuration With Propeller Power Effect," AIAA Paper 89-0560, Jan. 1989.

[25]Hess, J. L. and Valarezo, W. O., "Calculation of Steady Flow About Propellers Using a Surface Panel Method," *Journal of Propulsion and Power*, Vol. 1, Nov.–Dec. 1985, pp. 470–476.

[26]Hess, J. L. and Valarezo, W. O., "Calculations of Steady Flowfields Using a Surface Panel Method," Douglas Aircraft Co., Rept. MDC J3914, Jan. 1986.

[27]Hess, J. L., "The Problem of Three-Dimensional Lifting Flow and its Solution by Means of Surface Singularity Distribution," *Computer Methods in Applied Mechanics and Engineering*, Vol. 4, Nov. 1974, pp. 283–319.